Supplementary Information

Climate response function for global mean surface temperature, P_{GS}

Outline discussion of modeling procedure

In previous work, top of the atmosphere measurements of global temperature forcing following the Mt Pinatubo eruption in 1991, together with climate model simulations, have suggested (Hansen 2005) that effective global temperature forcing by stratospheric aerosols, F_e, and stratospheric optical depth, τ, are related by F_e (W m^{-2}) ~ –23 τ. It has also been shown that the large reduction in F_e following the Mt Pinatubo eruption led to a 0.7°C peak decrease in ENSO-corrected T_{LT} (Soden 2002). However, as Fig. S1(b) shows, the corresponding peak decrease in ENSO-corrected T_{GS} was about a factor 2 smaller, in contrast to climate model simulations. In the following paragraphs I will compare the post-eruption evolution of $\overline{T}_{\mathrm{LT}}$ and $\overline{T}_{\mathrm{GS}}$, where the bars denote ENSO-corrected quantities, in order to estimate and compare the transient climate response functions $P_{\mathrm{LT}}(t)$ and $P_{\mathrm{GS}}(t)$ for these two interrelated parts of the global climate system.

Modelled changes in radiative forcing by volcanic aerosols and solar irradiance during the period 1960–2000, together with ENSO-corrected satellite measurements of lower troposphere temperature during the Mt Pinatubo event (Soden 2002), are shown in Fig. S1(a). The symbols represent temperature measurements and the dashed line shows the time-dependent forcing estimated from stratospheric optical depth (NASA 2018) and solar irradiance data (NOAA 2018). In order to fit the temperature data, the forcing data are convoluted with a trial climate pulse-response function for the lower troposphere, $P_{\mathrm{LT}}(t)$, based on the intermediate climate model response of Hansen *et al*. (2017), defined during years 1–10 as $P_{\mathrm{LT}} = 0.1737/t$. To adequately fit the climate response at times < 1 y this curve is extended back to $t = 0$, with a cut-off P_{LT} = 0.6 y^{-1} at t < 0.25 y to match the observed temperature drop at the peak of cooling after the Mt. Pinatubo eruption. The equilibrium climate response of 0.75°C / W cm^{-2} used by Hansen *et al*. (2017) is preserved by downscaling $P_{\mathrm{LT}}(t)$ at times after the initial cut-off by a factor ~1. The model uses a forcing of F_e(W m^{-2}) = 21 τ to fit the observed magnitude of the temperature response. The resulting temperature evolution, obtained by convoluting F_e with P_{LT} (details in the Supplementary Information) is given by the solid curve in Fig. S1(a).

Fig. S1(b) shows the corresponding response of $\overline{T}_{\mathrm{GS}}$ to the same forcing evolution. For clarity the plot has been background-subtracted to offset the average growth in global temperature during this period, which is largely of anthropogenic origin. It is clear that the surface temperature response is strongly damped in comparison to the troposphere response (dashed curve in Fig. S1(b)). This is perhaps not surprising as global mean surface temperature is known to be damped by the buffering influence of the ocean (Hansen 2017). However, the early transient response (during the first 2–3 y after eruption) is also significantly weaker than predicted by climate models, e.g. Hansen *et al*. (2017) (symbols).

The damping introduced by the ocean cannot be treated as a straightforward smoothing of temperature response. In the initial 1–2 years after the Mt Pinatubo eruption there is a prompt response with a steep drop in $\overline{T}_{\mathrm{GS}}$, but the magnitude of this decrease is smaller than that in $\overline{T}_{\mathrm{LT}}$. On the other hand, the tail of the temperature response appears to be stronger than that of $\overline{T}_{\mathrm{LT}}$, consistent with the thermodynamic requirement that the cumulative troposphere and global surface responses converge as the atmosphere-ocean system relaxes towards equilibrium. This suggests that

the climate response function for the global mean surface may differ significantly from that used in existing climate models. The challenge here is to be able to model both the troposphere and global surface temperature responses satisfactorily, using a single common volcano forcing time series, consistent with thermodynamics.

In principle, a straightforward method of extracting an observationally-based global mean surface temperature response function would be to invert the temperature time-series data using the volcano forcing (stratospheric optical depth) time series as input. However, this approach has practical difficulties as the long-term temperature background generated by other forcings (greenhouse gases, aerosols, etc) is not exactly known, and any systematic variations may misdirect a statistically-based inversion.

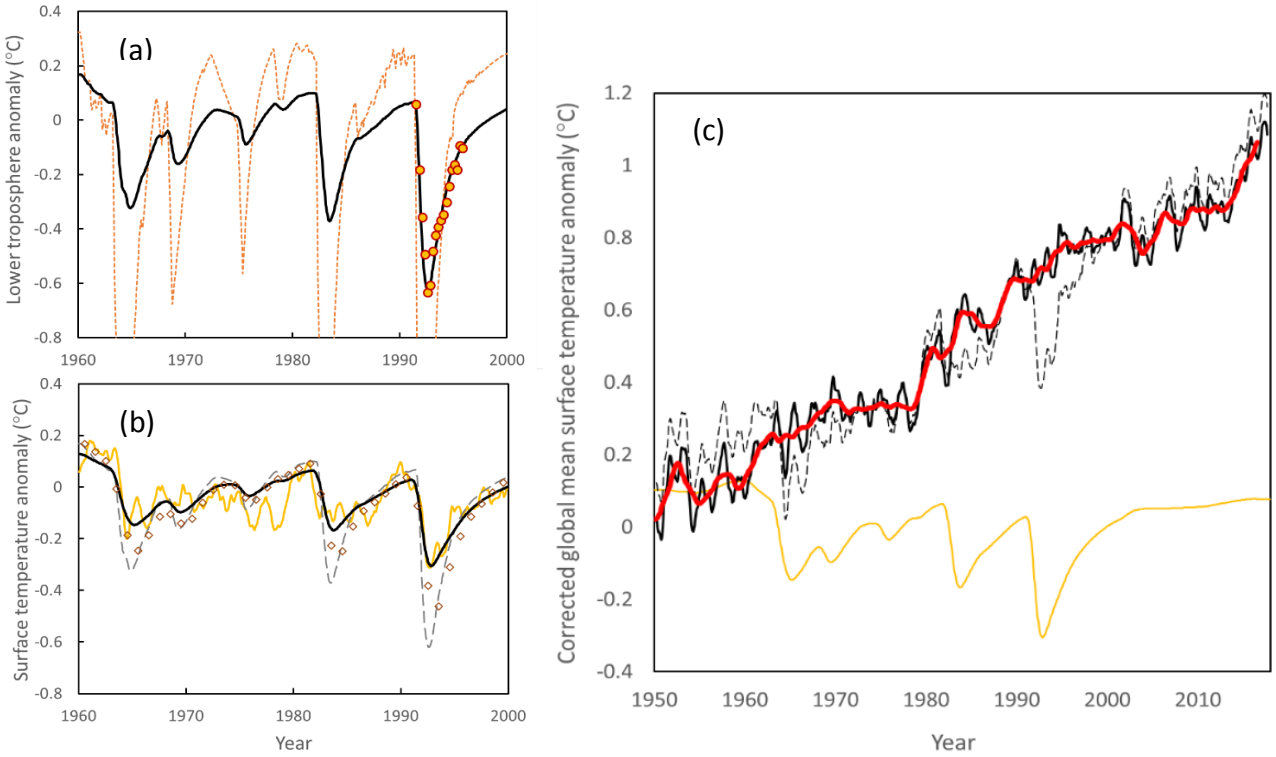

Fig. S1: (a) Climate forcing by volcanic aerosols and solar irradiance variations between 1960 and 2000 (dashed curve) and the resulting temperature evolution of the lower troposphere (solid black curve) obtained by convoluting the forcing data with P_{LT}. Symbols represent satellite measurement data. (b) Global mean surface temperature evolution obtained by the same method (solid black curve) using the updated response function P_{GS}. The dashed curve in (b) is the tropospheric response and symbols denote the time series calculated from the annual forcings and global surface response function used by Hansen *et al*. (2017). The gold line represents $\overline{T}_{\mathrm{GS}}$ after subtracting a linear background representing the rising temperature trend from anthropogenic emissions. (c) Historical evolution of $\overline{T}_{\mathrm{GS}}$ (dashed line), the temperature response to volcano and solar irradiance variations (gold solid line), and $\overline{T}_{\mathrm{GS}}$ after removal of the volcano and solar contributions (black solid line). The red curve shows the corresponding result after suppression of quasi-biennial oscillations using a 26-month running mean. The recent increase in slope indicates a steep rise in anthropogenic global temperature forcing, confirming the trend seen in Fig. 1 of the paper.

Here a physically motivated approach is used to construct the trial climate response function, P_{GS}, which is then optimized. At short times P_{GS} is assumed to be a function of the troposphere response,

P_{LT}, partially modified by thermal interaction with the ocean, and at sufficiently long times the function is based on that of Hansen *et al*. (2017), expressed here in the pulse-response form $P_{\mathrm{GS}} = a_n/t$ where a_n is a constant with values for n = 1–3 specified in the ranges t < 10 y, 10 y ≤ t < 100 y, 100 y ≤ t < 2000 y, respectively. The a_n values are scaled by a factor ~1 to compensate for the modification to the response function at short times, so that, as with the troposphere, the equilibrium climate response remains equal to 0.75°C / W m^{-2} (see detailed discussion in the sub-section below).

Two distinct subsets of the global surface have radically different thermal properties. In the first, primarily land and sea-ice areas, the heat flux through the surface is much weaker than that into the open ocean, as thermal diffusion below the surface is slow. As a result, the surface in these areas acts similarly to a Neumann boundary. In contrast, the ice-free global ocean is a powerful source/sink of heat with a mixed boundary condition for tropospheric heat and can thus maintain a significantly different surface temperature anomaly from that of the troposphere. The result is a land surface temperature anomaly that is roughly similar to that of the lower troposphere and a sea-surface temperature anomaly T_{SS} that is somewhat smaller – intermediate between the land and ocean anomalies. Thus $T_{\mathrm{GS}} \approx \alpha T_{\mathrm{LT}} + (1-\alpha)T_{\mathrm{SS}}$, where $\alpha = 0.31$ is the fraction of Earth's surface occupied by land and sea ice.

It is therefore appropriate to model P_{GS} in terms of two components: $P_{\mathrm{GS}} = \alpha' P_{\mathrm{LT}} + (1-\alpha')P_{\mathrm{SS}}$. In the first component, P_{LT} is the lower troposphere response and α' is a free parameter which should be similar to α. In the second component, P_{SS} is a modification of P_{H} in Ref. 7 obtained by truncating P_{H} to a maximum value of 0.038 y^{-1}, creating a plateau response at times shorter than 2.5 y. This strongly reduces the magnitude of the initial global surface response while the term $\alpha' P_{\mathrm{LT}}$ maintains its initial sharp response, as shown in Fig. 2(b).

With this approach the post-eruption evolution of T_{LT} (Fig. 2a) and T_{GS} (Fig. 2b) can be consistently modeled using the same global temperature forcing time series. The fitted value of α', which is constrained by the relative contributions to T_{GS} of the initial sharp volcano response and the longer response tail, lies in the range 0.35–0.45, slightly larger than α. This modest discrepancy may arise from transient sea-surface warming prior to mixing of the added heat into the epipelagic zone. Still, it is clear that the sea surface response in the second term of P_{GS} varies more slowly than the trend in P_{H} after an initial forcing pulse. This slower response may, for example, reflect faster epipelagic mixing than is assumed in most climate models. The key point for this work is that P_{GS} gives a satisfactory fit to the volcano dips shown in Fig. 2(b) and thus an improved semi-empirical estimate of global mean surface temperature response which can be applied to volcano and solar irradiance forcings (and in principle to other forcings as well).

Model analysis

Climate response functions for different components of the climate system differ according to their thermal mass and strength of coupling with other components. In this work the responses of the lower troposphere and global mean surface to volcano and solar forcing on time scales ~1-20 y have been fitted to the time series T_{LT} reported by Soden *et al*. (2002) and $\overline{T}_{\mathrm{GS}}$ reported in this work, respectively. For this purpose, the multi-decadal time series $\overline{T}_{\mathrm{GS}}$ is fitted after background subtraction to remove the slowly-varying, approximately linear, contribution from anthropogenic temperature rise.

The fitting function, representing the response of global mean surface temperature to volcano and solar forcings, is of the form

$$T(t) = \lambda \sum P_{\mathrm{GS}}(t') F_e\,(t - t')\Delta t' \tag{S1}$$

where the sum runs over monthly time points (thus $\Delta t = \frac{1}{12}$ y) from January 1850 to the present and a mid-range climate sensitivity $\lambda = 0.75$°C / W m^{-2} is used. Here

$$P_{\mathrm{GS}} = \alpha' P_{\mathrm{LT}} + (1 - \alpha') P_{\mathrm{SS}} \tag{S2}$$

where α' is an adjustable parameter that approximately represents the fraction of Earth's surface occupied by land and sea ice, and P_{LT} and P_{SS} are given by

$$\begin{aligned} P_{\mathrm{LT}}(t) &= a_0^{\mathrm{LT}} \qquad \left(0 < t \le t_1^{\mathrm{LT}}\right) \\ P_{\mathrm{LT}}(t) &= a_n^{\mathrm{LT}}/t \quad \left(t_n^{\mathrm{LT}} < t < t_{n+1}^{\mathrm{LT}}\right) \end{aligned} \tag{S3}$$

$$\begin{aligned} P_{\mathrm{SS}}(t) &= a_0^{\mathrm{SS}} \qquad \left(0 < t \le t_1^{\mathrm{SS}}\right) \\ P_{\mathrm{SS}}(t) &= a_n^{\mathrm{SS}}/t \quad \left(t_n^{\mathrm{SS}} < t < t_{n+1}^{\mathrm{SS}}\right) \end{aligned} \tag{S4}$$

and the values of a_n^{LT} and a_n^{SS} are derived from prior values used by Hansen *et al*. (2017), modified as described below. The times t_n $(n < 0)$ for both lower troposphere and global surface temperature are kept at the values used in Ref. (Hansen 2017). The complete set of adjusted values of a_n and t_n is given in Table S1.

The forcing $F_e = F_e^{\mathrm{volcano}} + F_e^{\mathrm{solar}}$ represents the sum of volcano and solar forcings, where the volcano contribution is derived from global time series data for stratospheric optical thickness, τ, (NASA 2012) using a forcing efficiency η such that $F_e^{\mathrm{volcano}} = \eta\tau$, and the forcing F_e^{solar} is derived from solar irradiance data, applying a geometrical correction of 0.25 and an albedo correction of 0.7 (Lean 2001). Estimates based on the monthly solar irradiance data held by NOAA (2018) agree closely with the annualized solar forcing estimates used by Hansen *et al*. (2017), suggesting that the latter also represent direct radiative forcing. However, as they were used by Hansen et al. (2017) as effective forcing values it appears that the effect of secondary infrared radiative forcing on the solar forcing contribution may have been neglected. Here it is assumed that secondary radiative forcing is a fraction -0.45 of direct radiative forcing, consistent with the ratio of secondary to direct stratospheric aerosol forcing reported by Hansen *et al*. (2005). Thus, the estimate of effective solar forcing used in this work is $0.55\times$ that used by Hansen et al. (2017). This correction has only a small impact on the results: for example, had it not been included, the black solid curve in Fig. (c) would have shifted downward by ≤ 0.03°C. The impact on decadal changes this century is ~ 0.01°C. The correction likewise only has a minor impact on the results in Hansen's 2017 paper.

The fit to T_{LT} in Fig. 2(a) of the paper, reproduced here as Fig. S1(a), is obtained by adjusting η in the expression for F_e and t_1^{LT} in the expression for P_{LT} with a corresponding adjustment to a_1^{LT} to maintain continuity at time $t' = t_1^{\mathrm{LT}}$. The remaining a_n^{LT} are adjusted by a common factor to preserve the normalisation $\sum P_{\mathrm{LT}} = 1$. The extracted values are $\eta = (21 \pm 2)$°C τ^{-1}/ W m^{-2} and $t_1^{\mathrm{LT}} = (0.25 \pm 0.05)$y. Uncertainty in η is associated with the area of the temperature dip in Fig.

S1(a) and originates mainly from potential systematic climatic variations in the lower troposphere temperature background during and after the Mt Pinatubo eruption, which although corrected for ENSO (Soden 2002) may also be influenced by QBO. Similar considerations may apply to previous analysis (Hansen 2005) based on measurements of primary and secondary radiative forcings, as the latter is also influenced by global temperature.

Within the uncertainties the present result agrees with the estimate of $\eta \approx 23°\text{C } \tau^{-1}$/ W m^{-2} from Hansen et al. (2005). This is interesting, as what is really determined here is the product $\eta\lambda$ which relates stratospheric optical depth, τ, to temperature response, $T(t)$, whereas Hansen's 2005 paper determined η. This is significant support for the mid-range climate sensitivity $\lambda \approx 0.75°\text{C}$ / W m^{-2}, assuming that the long-term response tail is adequately described by Hansen's response function.

The uncertainty in t_1^{LT} is associated with the depth of the dip in Fig. 1(a) which is also mainly affected by unknown variability in the background troposphere temperature, in this case during the time interval around the minimum in stratospheric optical depth following the eruption. The estimated uncertainty in t_1^{LT} corresponds to a ~10% uncertainty in the depth of the temperature minimum.

Having established an estimate for η based on the lower troposphere data, the resultant volcano forcing is used together with the solar forcing time series discussed above to fit the time evolution $T(t)$ of background-subtracted global mean surface temperature, in order to extract $P_{\mathrm{GS}}(t)$. Prior values in the equations for the P_{SS} contribution to P_{GS} are treated in the same manner as above. Fitting parameters are the fraction α' and the time t_1^{SS} at which the initial plateau response in equation (S4) reverts to the $1/t$ trend. The extracted values are $\alpha' = 0.4 \pm 0.05$ and $t_1^{\mathrm{SS}} = (2.4 \pm 0.5)$ y. The uncertainties in the extracted values of α' and t_1^{SS} mainly arise from the unknown time evolution of the QBO in the background of the three volcano dips shown in Fig. S1(b) of the paper, thus the extracted optimal values and uncertainties are partly subjective. However, it is clear from Fig. S1 (b) that the optimal fit gives substantially improved agreement with the historical time series for background-subtracted $\overline{T}_{\mathrm{GS}}$. Moreover, subtraction of $T(t)$ from the $\overline{T}_{\mathrm{GS}}$ time series in Fig. S1(c) leaves no residual evidence of artefacts such as volcano dips or peaks, suggesting that the function $T(t)$ accurately represents the effects of volcano and solar variations over the period of interest. For example, subtraction of the largest dip, associated with the 1991 Mt Pinatubo eruption, leaves only small quasi-biennial fluctuations in the remaining temperature evolution (black solid curve) during the period from 1990–1995.

Table 1: Adjusted values of a_n and t_n in units of y^{-1} and y, respectively, used in the expressions for P_{LT} and P_{GS}. Uncertainties for the fitted parameter t_1 are shown in brackets. Values for t_2–t_4 are from Hansen (2017).

	a_0	a_1	a_2	a_3	t_1	t_2	t_3	t_4
P_{LT}	0.6	0.13	0.086	0.083	0.25 (0.05)	10	100	2000
P_{SS}	0.038	0.16	0.11	0.106	2.4 (0.5)	10	100	2000

Earth system temperature metric, θ

Global temperature fluctuations arising from heat exchange between ocean and atmosphere can be eliminated, in the framework of a simple climate model description, by considering an effective temperature metric, θ, which includes contributions from global mean surface temperature, T_{GS}, and upper ocean heat content, H_{UO}. In order to capture cyclical heat-transfers involved in decadal

processes such as the PDO and shorter-duration cycles such as ENSO and the QBO, it is necessary to choose a sufficiently deep upper-ocean layer that fully contains these processes. Data from the Argo network re-analysed by Cheng et al. (2017) show that ocean depths below 700 m have warmed approximately linearly since the mid-1990s, with no significant fluctuations in the warming rate during this time. Thus, the depth range 0–750m appears sufficient to capture all significant ocean–atmosphere heat cycling processes at time scales up to 1–2 decades. At the same time, in order to avoid an excessively heavy-tailed climate response for the function θ, it is desirable to choose an upper ocean layer that is as shallow as possible. The depth range 0–750 m is thus well suited as the upper ocean depth in the formulation of θ.

The quantities T_{GS} and H_{UO} both include a contribution from global temperature forcing and a contribution from heat exchange between the upper ocean and atmosphere. Since heat leaving the ocean goes predominantly to the lower troposphere, one may write

$$\Delta H = C_A T_{LT} \tag{S5}$$

where ΔH is the excess heat that has been transferred from ocean to atmosphere relative to normal globally forced climate response, and C_A is an effective heat capacity for the atmosphere.

As discussed in the manuscript, $T_{GS} \approx \alpha T_{LT} + (1-\alpha) T_{SS}$. Since T_{LT} is large compared to T_{SS}, the term involving T_{SS} may conveniently be neglected in the heat transfer term, which itself is small compared to climate forcing. Neglecting radiative losses from the atmosphere in the first instance, this approximation leads to

$$T_{\mathrm{GS}} = \lambda P_{\mathrm{GS}} * F_e + \alpha \frac{\Delta H}{C_A} \tag{S6}$$

$$T_{\mathrm{UO}} = \Lambda P_{\mathrm{UO}} * F_e - \frac{\Delta H}{C_{\mathrm{UO}}} \tag{S7}$$

where $P * F_e$ denotes the convolution $\int P(t') F_e(t-t') dt'$, λ is the equilibrium climate response for global mean surface temperature, Λ is the equilibrium response for upper-ocean temperature $T_{\mathrm{UO}} = H_{\mathrm{UO}}/C_{\mathrm{UO}}$, and C_{UO} is the heat capacity of the upper ocean.

When radiative losses are included, variations in T_{LT} are significantly reduced. This is accounted for here by applying a scaling factor $1-\gamma$, where γ represents the radiative losses, leading to

$$T_{\mathrm{GS}} = \lambda P_{\mathrm{GS}} * F_e + (1-\gamma)\alpha \frac{\Delta H}{C_A} \tag{S6'}$$

The equilibrium response Λ in equation (S7) can be formulated in terms of λ by considering the temperature distribution as a function of depth, $T(z)$. In the simple fast climate model framework, the temperature at the bottom of the ocean is implicitly assumed constant while the equilibrium temperature anomaly at depth z (and height h in the atmosphere above) is proportional to the forcing. Consequently

$$\Lambda = \rho\lambda$$

where $\rho = (T_{\mathrm{UO}}/T_{\mathrm{GS}})_{eq}$ is the equilibrium ratio between T_{UO} and T_{GS}, determined by the heat transport properties of the ocean-atmosphere system.

The heat exchange terms can be eliminated by adding equations (S6') and (S7):

$$T_{\mathrm{GS}} + (1-\gamma)\alpha\frac{C_{\mathrm{UO}}}{C_A}T_{\mathrm{UO}} = \lambda\left(P_{\mathrm{GS}} + (1-\gamma)\alpha\rho\frac{C_{\mathrm{UO}}}{C_A}P_{\mathrm{UO}}\right) * F_e$$

which can be expressed as

$$\theta = \lambda P_\theta * F_e \tag{S8}$$

where

$$\theta = \left(T_{\mathrm{GS}} + \frac{(1-\gamma)\alpha}{\epsilon}T_{\mathrm{UO}}\right)\Big/\left(1 + \frac{(1-\gamma)\alpha\rho}{\epsilon}\right)$$

$$P_\theta = \left(P_{\mathrm{GS}} + \frac{(1-\gamma)\alpha\rho}{\epsilon}P_{\mathrm{UO}}\right)\Big/\left(1 + \frac{(1-\gamma)\alpha\rho}{\epsilon}\right)$$

with $\epsilon \approx C_A/C_{\mathrm{UO}}$, and $T_{\mathrm{UO}} = H_{\mathrm{UO}}/C_{\mathrm{UO}}$. The function θ is an effective temperature metric representing the evolution of heat in the combined atmosphere-upper ocean system. It is thus in principle directly related to forcing without interference from internal climate variability.

The heat capacities of the atmosphere and the 0–750 m upper ocean are approximately 6.0×10^{21} J K^{-1} and 1.1×10^{24} J K^{-1}, respectively, which implies $\epsilon \sim 0.0055$. The value of α is set to 0.31, the average area of land and sea ice, and γ is assumed equal to 0.45. Then,

$$\theta = (T_{\mathrm{GS}} + 31\,T_{\mathrm{UO}})/(1 + 31\rho)$$

To enable consistency between the T_{GS} and T_{UO} time series, OHC data must be referred to the same baseline period as is used for T_{GS}. Since OHC data are not available for the T_{GS} baseline period 1880–1920, the time series data reported by the Japan Meteorological Agency (2018) are offset from their reported 1981–2010 baseline by -9×10^{22} J, thus placing the baseline just below the reported minimum in OHC between 1968 and 1970. This choice appears reasonable as T_{GS} has minima in the 1950s and 1960s which are just above its 1800–1920 baseline.

A value of $\rho = 0.141$ is estimated from

$$\rho = \left(\frac{T_{\mathrm{UO}}}{T_{\mathrm{GS}}}\right)_{eq} \approx \frac{\langle T_{\mathrm{UO}}\rangle}{\langle T_{\mathrm{GS}}\rangle}$$

where the triangular brackets represent mean values for the period 2005–2011. This rough equality may slightly underestimate ρ because the climate response of T_{UO} lags a few years behind that of T_{GS}. However, it has the advantage that the curves for T_{GS} and θ can be conveniently overlaid and compared visually. With these parameters the equation for θ becomes

$$\theta \approx A\,T_{\mathrm{GS}} + B\,T_{\mathrm{UO}}$$

where $A = 0.195$ and $B = 5.78$. Fig. S2 shows the resultant time series for θ and the contributing terms in AT_{GS} and BT_{UO}, together with the uncorrected T_{GS} curve for comparison.

Owing to the large contribution from the upper ocean, θ has a heavy-tailed distribution that makes its response to forcing smoother than that of T_{GS}. However, fast diffusion within the epipelagic zone, which is typically around 300 m deep – nearly half the depth of the 0–750 m upper-ocean depth considered here – may produce a significant upper ocean temperature response on the timescale of 2-3 years identified in the previous section. This can be expected to generate a gradually steepening slope of the T_{UO} term since 2012, in addition to the sharp increase in slope of the T_{GS} term.

The recent 5-year period has been too short to allow definitive confirmation of an increase in slope of the T_{UO} term, but the combination of analyses by Ishii (2009) used in the Japan Meteorological Agency data (2018) and by Cheng *et al*. in their 2017 paper is consistent with this hypothesis, with the ocean curve rising noticeably above its initial trend (blue dotted line) after 2012.

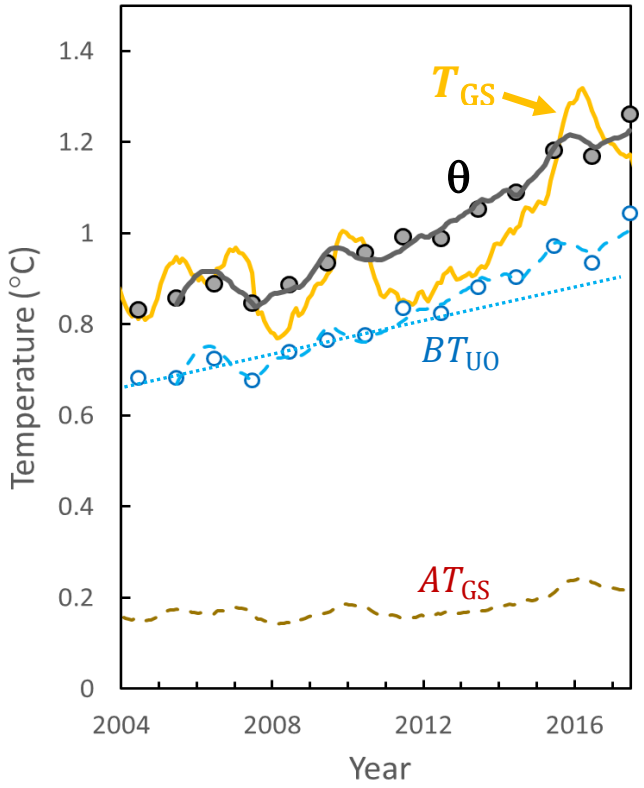

Fig. S2: Time series for T_{GS} (gold curve), θ (black solid curve and symbols) and its components AT_{GS} (red dashed curve) and BT_{UO} (blue dashed curve and symbols), during the Argo period. Symbols are based on data from Ishii et al. (Ishii, JapMet) and the blue and black curves are based on the OHC data of Cheng et al. (Cheng 2017, Cheng 2018) with a baseline offset chosen to match the two datasets during the period since 2005. The dotted line is a straight-line fit to the scaled upper-ocean data (BT_{UO}) from 2004–2010, indicating a possible recent increase in the rate of ocean warming.

Moreover, it is clear that

(a) there has not been the prompt decrease in the slope of T_{UO} which a transition to warmer atmospheric and cooler ocean conditions would require[†]

(b) the combined ocean-atmosphere response represented by θ is on a steepening curve that reflects an increase in forcing F_e.

The above analysis benefits from simplicity but has some potential limitations due to its reliance on a simple fast-climate model. It includes a correction for variations in outgoing infrared radiation caused by atmospheric temperature change, but does not account for forcing variations arising from changing atmospheric water content and other climatic variables that play out in three dimensions within the ocean-atmosphere system, particularly on short time scales. The neglect of an explicit sea-surface temperature contribution to the second term in equation S2' may also have a noticeable effect on θ. A combination of these issues may account for the slight shift in timing between ocean temperature decrease and global mean surface temperature rise during the two El Niño events visible in Fig. S2, in 2010 and 2015/16, which lead to a small peak (dip) in θ at the start (end) of each event, especially in the second, larger event. However, such effects are of second order in comparison to the gross heat-exchange effects accounted for by θ. In the period of accurate ocean temperature measurements initiated by the current Argo experiment, the θ-metric may be of value in focusing attention on the whole Earth system as a monitor of decadal forcing changes.

_____

[†] Such a decrease would not be smoothed by climate response inertia because it arises from heat transfer, not forcing (see second term in equation (S7)).

References

Cheng, L., Trenberth, K. E., Fasullo, J., Boyer, T., Abraham, J. & Zhu, J. Improved estimates of ocean heat content from 1960 to 2015. Sci. Adv. **3**:e1601545 (2017).

Cheng, L. Private communication (2018).

Hansen, J. *et al.* Efficacy of climate forcings. J. Geophys. Res. **110**, D18104 (2005).

Hansen, J. *et al*. Young people's burden: requirement of negative CO_2 emissions. Earth. Syst. Dynam. **8**, 577-616 (2017).

Ishii, M. & Kimoto, M. Reevaluation of historical ocean heat content variations with time-varying XBT and MBT depth bias corrections. J. Oceanogr. **65**, 287–299 (2009)

Japan Meteorological Agency, Global ocean heat content, URL: http://www.data.jma.go.jp/gmd/kaiyou/english/ohc/ohc_global_en.html (May 2018).

Lean, J. L. Solar irradiance and climate forcing in the near future. Geophys. Res. Lett. **28**, 4119-4122 (2001).

NASA GISS Global Mean Optical Depths. NASA Goddard Institute for Space Studies, URL: https://data.giss.nasa.gov/modelforce/strataer/tau.line_2012.12.txt , accessed June 20, 2018

NOAA solar irradiance Climate Data Record (2018) URL: https://www.ncdc.noaa.gov/cdr/atmospheric/total-solar-irradiance

Soden, B. J., Wetherald, R. T., Stenchikov, G. L. & Robock, A. Global cooling after the eruption of Mount Pinatubo: a test of climate feedback by water vapor. Science **296**, 727 (2002).